Ocean Engineering 267 (2023) 113224

Contents lists available at ScienceDirect

Ocean Engineering

journal homepage: www.elsevier.com/locate/oceaneng

Hydro-optic interaction study on submerged unmanned underwater vehicles regarding to Snell's window

Shayan Rabizadeh, Ali Esmaeili *

Mechanical Engineering Department, Engineering Faculty, Ferdowsi University of Mashhad, Iran

ARTICLE INFO

Keywords:
Hydrodynamic
Optic
Submerged hydrofoil
Unmanned underwater vehicle
Snell's window

ABSTRACT

The underwater creatures have always desired to collect information about what is in beyond, for instance, the fishes that hunt birds with precise calculations. Possessing a subsurface device capable of imaging the outside area of water without any distortion can be notified of modern demand. To be acquainted with this phenomenon, a series of submerged hydrofoils with various geometrical properties are mentioned in different submerged distance and incidence angles to recognize the recondite limits upon its aberrated eyesight. The behavioral changes of the wave's surface have been numerically discussed in detail by ray length. The primary outcomes reveal that Snell's window varies under different conditions. In brief, the emitted ray undergoes more severe distortions when the hydrofoil is positioned near the water's surface. However, interestingly enough, other parameters such as hydrofoil's geometry, the angle of attack, and the flow's velocity affect the wave's shape, and that wave's geometry sets different distortions patterns in different areas that the camera spots.

1. Introduction

Nature has always been humankind's stimulation of opening new borders of science by observing the way of the astonishing creature called giant trevallies, a fish capable of locating the flying birds despite the aberration in the trajectory.

The fish focuses on the bird's velocity, flying altitude, and its own submerged depth while considering the aberration in its trajectory. These precise calculations would result in a successful hunt, as illustrated in Fig. 1.

As natural recording events are becoming more popular among environmentalists, a camera that can overcome the aberrations generated for some reason is highly required. There are numerous series of research done on optical distortion. The vast majority are aero-optical ones, which have been investigated in various test cases. First of all, aero-optics can be defined as a branch of science in which a lasering system triggers the distortions of an optical beam in an aircraft flight system. These aberrations are triggered by severe density gradients such as turbulences, turbulent boundary layers in both subsonic and supersonic flight conditions, mixing layers, and vortices from the viewpoint of fluid density and many other cases which make sudden changes that have significant influences on the ray's path and generate those distortions. In spite of the fact that aero-optics is considered one of the newly discovered fields of science, there are numerous researches done on this matter. Reducing the overall distortions of an optical beam is the objective of aero-optical mitigations, which can be achieved through a variety of flow control and adaptive-optics technique that has been reviewed by Wang et al. (2011). One of the interesting factors to study is the geometry of the case which is varied in different investigations. For instance, Shotorban et al. (2021) have studied the cylindrical turret and understood that the degradation phenomenon of the optical beam during its propagation through the boundary layer is characterized by the link between the flow boundary layer and shock layer, and the Mach number also affects aero-optical aberration, and in another work (Yu et al., 2021), an ellipsoidal dome is investigated and figured that image degradation is mainly caused by the conformal dome's index distribution in the aero-thermal environment. At the same time, the deformation's influence is relatively insignificant, and suppressing the aero-optical aberration of the conformal dome well could be done by the Wavefront coding technology. In the matter of heat transfer, Sun et al. (2021) studied film cooling via tangential wall injection and realized the existence of a universal contradiction regarding the mutual realization of both aero optical suppression and thermal protection. Working on turbulence and distortions have been popular among scientists and investigations such as (Sun and Liu, 2020) Aimed at reducing aero-optical effect, wall-bounded turbulent flows under different wall thermal conditions and wall blowing. Furthermore, Yang et al. (2021)

* Corresponding author.
E-mail address: aliesmaeili@ferdowsi.um.ac.ir (A. Esmaeili).

https://doi.org/10.1016/j.oceaneng.2022.113224
Received 21 July 2022; Received in revised form 6 October 2022; Accepted 17 November 2022
Available online 6 December 2022

Nomenclature

h	distance from water's surface
c	cord length
ϴ	deflection angle
t	hydrofoil thickness
Φ	scalar quantity
C_l	lift coefficient
Re	Reynolds number
p	Pressure
α	Volume fraction
ρ	density
g	Gravitational acceleration
K-w SST	turbulence model, a two-equation eddy-viscosity model
V	velocity vector
K_{GD}	Gladstone-Dale coefficient
n(r)	refractive index at the beam location
h	step size
d	distances between the points
C_P	pressure coefficient
AOA	Angle of attack
OPD	Optical path difference
OPL	Optical path length
F	Froude number
CFD	computational Fluid dynamics
Γ	diffusivity coefficient
T	stress tensor
I	stress tensorarea moment of inertia (m^4)
S	source term
I^c	Convection flux
I^D	Diffusion flux
$\dot{m}$	mass transfer
n_0	refractive index
x	horizontal cartesian parameter
y	vertical cartesian parameter
μ	dynamic viscosity

Fig. 1. Hunting procedure from the time the hunter catches the prey (Earth, 2014).

worked on wavefront distortions and proposed the idea of injecting a gas with an equal density of the used fluid at the vortex boundary for reducing distortions. Supersonic conditions are one of the reasons of distortions and is investigated by Ding et al. (2017). Sun and Liu(Sun and Liu, 2020) has investigated the plate with wavy roughness in high-Reynolds-number, they understood reducing the wall-normal grid resolution leads to an apparent spatial lag in the transitional position. Hypersonic conditions has been examined by Li et al. (2019) and acknowledge that the image degradation with lower Mach number is less obvious than higher Mach number, relatively. Interestingly enough a transient simulation is carried out by Yang et al. (2021).

As self-explanatory it is, all aero-optical aberrations in different test cases are the effect of density gradient in the flow that has been considered in most aero-optical issues. Despite the tremendous research done in this field, the bigger picture would be considering a multiphase approach. This case of study is highly dependent on gradient changes. A more exciting change is a severe one like water to air interior. However, before simulating the aberrations from water to air, there are some factors to consider. Firstly, the formed wave is one of the main factors affecting the aberration, which depends on critical parts like the hydrofoil thickness, submerged depth, the moving pace, and the angle of attack. Prediction of the wave's shape alterations is one of the many investigations conducted in marine engineering. Identifying wave shape behavior is a priority, a phenomenon that has been investigated before by Djavareshkian et al. (2013). They have concluded that the hydrofoil type does not affect wavelength. In another similar research Esmaeilifar et al. (2017) has denoted that the free surface affects trailing edge vortices and subsequently reduces transient momentum and thrust force for the critical frequency range and all frequencies of Submergence depth equal to 0.5. Another critical parameter for this matter is hydrofoil's performance that is carried by Djavareshkian and Esmaeili (Djavareshkian and Esmaeili, 2013). An similarly shape optimization and operating conditions of the submerged hydrofoil conducted (Djavareshkian and Esmaeili, 2014) pinpointed that the obtained configuration of hydrofoil in optimum operating conditions could reach a maximum lift to drag ratio. In more recent studies such as (Garg et al., 2019) delineated by given the thicker section, the higher load capacity, and the much-delayed cavitation inception characteristic of the optimized hydrofoil. The research (Xu et al., 2020) can identify the fact when the free surface is considered, the downstream hydrofoil moves in the wave flow and the wake flow of the upstream hydrofoil. The highest lift coefficient can be achieved when it is positioned at the following zero crossing with

upwash flow.

With all that being said, the juxtaposition of these two topics will be eminent; consequently, no investigation subsumes both areas. Moreover, this study focuses on overcoming various aberrations due to the density gradient in the water to air interior where the hydrofoil is placed to face eclectic conditions to identify the widest eyesight, known by Snell's window.

2. Governing equations and simulation formola

2.1. Fluid flow equations

The basic equations, which describe the conservation of mass, momentum, and scalar quantities can be expressed in the following vector form, which is independent of the coordinate system:

$$\frac{\partial \rho}{\sigma t} + div\left(\rho \overrightarrow{\mathrm{V}}\right) = \mathrm{S_m} \tag{1}$$

$$\frac{\partial\left(\rho \overrightarrow{\mathrm{V}}\right)}{\partial t} + div\left(\rho \overrightarrow{\mathrm{V}} \otimes \overrightarrow{\mathrm{V}} - \overrightarrow{\mathrm{T}}\right) = \overrightarrow{\mathrm{S}}_v \tag{2}$$

$$\frac{\partial(\rho \varnothing)}{\partial t} + div\left(\rho \overrightarrow{\mathrm{V}}\, \varnothing - \overrightarrow{\mathrm{q}}\right) = \overrightarrow{\mathrm{S}}_{\varnothing} \tag{3}$$

and as it is gathered from fluid mechanics, the Newtonian flow's stress tensor would be:

$$\overrightarrow{\mathrm{T}} = -P\ \overrightarrow{\mathrm{I}} \tag{4}$$

More on that the Fourier-type law for the scalar flux vector will be followed as:

$$\overrightarrow{\mathrm{q}} = \Gamma_{\varnothing} grad \varnothing \tag{5}$$

For solving this problem, To stimulate turbulence in low Reynolds number flows the $k-w$ *SST* flow model is used (Field, 1994). This turbulent model uses the standard $k-w$ boundary layer model as inner part of the boundary layer, so no relaxation factor is needed while in the outer part of the model, the $k-\varepsilon$ Standard model has no sensitivity problem to free stream as does the $k-w$ model. the $k-w$ *SST* model was chosen for the turbulence flow. Finite-volume approach was applied to discretize the above differential equation. Firstly, the solution domain is divided into a finite number of discrete volumes or cells, where all variables are stored at their geometric centers. Then, the Gaussian theorem is used to integrate the equations over all the control volumes. The discrete expressions are presented to refer to only one face of the control volume, namely, e, for the sake of brevity. For any variable Φ (which may also stand for the velocity components), the result of the integration yields:

$$\frac{\delta v}{\delta t}\left[(\rho\varphi)_p^{\,n+1} - (\rho\varphi)_p^{\,n}\right] + I_e - I_2 + I_n - I_s = S_{\varphi}\delta v \tag{6}$$

Where, $I's$ is the combined cell-face convection I^c and diffusion I^D flux. The diffusion flux is approximated by central differences. The discretization of the convective flux requires special attention and it causes to develop the various schemes. A representation of the convective flux for cell-face (e) is:

$$I_e^c = (\rho.V.A)_e \varnothing_e = F_e \varnothing_e \tag{7}$$

The value of Φ_e is not known and should be estimated from the values of neighboring grid points by interpolation. The expression for the Φ_e is determined by second order Upwind scheme. The final form of discretized equation from each approximation is given as:

$$A_p\, \varnothing_p = \sum_{m=E,W,N,S} A_m\, \varnothing_m + S'_{\Phi} \tag{8}$$

That $A's$ are the convection-diffusion coefficients. The term S'_{Φ} in Eq. (8) contains quantities arising from non-orthogonality, numerical dissipation terms and external sources. For the momentum equations, it is easy to separate out the pressure gradient source from the convection momentum fluxes.

Volume of fluid (VOF) ideas have been utilized to simulate two-phase fluid (water and air). The VOF model can model two or more immiscible fluids by solving a single set of momentum equations and tracking the volume fraction of each of the fluids throughout the domain. It is considered that the SST k-w model simulates turbulent flow. Second-order schemes with restrictive features are used to discretize convection terms. As a result of the free surface, the flow is volatile near the free surface. Therefore, choosing a one-order scheme will keep solving stability stable, but accuracy will be significantly impacted. As a result, a bounded second-order scheme is guaranteed to be stable and accurate. Euler's one-order scheme and Van Leer's second-order scheme discretize the terms of time and VOF equation, respectively. The tracking of the interface between the phases is accomplished by the solution of a continuity equation for the volume fraction of one of the phases. For the q_{th} phase, this equation has the following form:

$$\frac{1}{\rho}\left[\nabla.\left(\alpha_q \rho_q v\right) = S_{pq} + \sum_{p=1}^{n}\left(\dot{m}_{pq} - \dot{m}_{qp}\right)\right] \tag{9}$$

where $\dot{m}_{pq}$ is the mass transfer from phase q to phase p, and $\dot{m}_{qp}$ is the mass transfer from phase p to phase q. S_{pq} is the source term which in this problem is mentioned as zero. The volume fraction equation will not be solved for the primary phase. The primary-phase volume fraction will be computed based on the following constraint:

$$\sum_{q=1}^{n} \alpha_q = 1 \tag{10}$$

The volume fraction equation may be solved either through implicit or explicit discretization. In this research, implicit is used.

2.2. Ray tracing methods

The index of refraction for air is linearly related to density through the Gladstone–Dale relation, (Guo et al., 2016) and (YANG et al., 2020) which can be expressed as:

$$n(r) = K_{GD}\rho(r) + 1 \tag{11}$$

where KGD is the Gladstone–Dale coefficient that is slightly influenced by the light wavelength. In addition, $\boldsymbol{r} = x\boldsymbol{i} + y\boldsymbol{j} + z\boldsymbol{k}$, which are the coordinates in the flow field. The integral of density along the path is defined as the optical path length (OPL), whose expression is shown below,

$$OPL(x', y', t) = \int_0^L n(x', y', z')dz' \tag{12}$$

where x ′ and y ′ are optical coordinates in the aperture plane, and z ′ is along the beam emitting direction. Then, in relatively short-length propagation, the wave-front distortion is quantified by the relative difference in the OPL, namely, the optical path difference (OPD),

$$OPD(x', y') = OPL(x', y') - [OPL(x', y')] \tag{13}$$

where the angle brackets denote the planar average, it should be stressed that the arithmetic mean of OPL is fully kept to take Zernike polynomial fitting directly for OPD. Each term of a Zernike polynomial for wavefront aberrations represents the isolated individual error since Zernike polynomials are defined orthogonally on a unit circle. Time-series analyses for lower-order errors (piston, tilts) determine the bandwidth requirements for the fast-steering mirror, and higher-order errors (defocus, coma, astigmatism, etc.) facilitate the design of the deformable mirror. Since the objectives are not leading to adaptive optical systems,

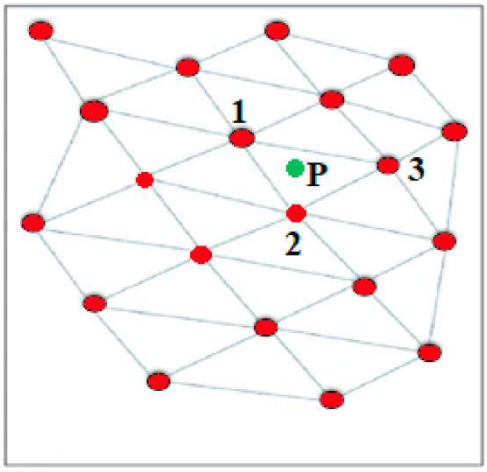

Fig. 2. Schematic of how the refractive index value is inserted using the vertices of a triangular grid created by the Delaney interpolation method.

the time series of Zernike polynomials are treated from a time-averaged rather than time-frequency aspect in this study. A Zernike polynomial with terms is currently utilized to fit any circular wave-front OPD, and a desirable degree of precision has been obtained. After calculating the refractive index field, the beam tracking was performed using the refractive field based on the obtained, and then the light deflection was plotted based on the radiation equation.

$$\frac{d}{ds}\left(n(r)\frac{dr}{ds}\right)=\nabla n(r) \tag{14}$$

Where r represents the position vector of the path of the beam unit, $n(r)$ is the refractive index at the beam location and ds is the length of the path increase, $\nabla n(r)$ is the slope of the refractive index at the beam location r, and $\frac{dr}{ds}$ represents the unit vector in the tangential direction along the propagation path. By defining a new variable as $t=\int\frac{ds}{dn}$ and as a result, $=\frac{ds}{n}$, the Eq. (15) is simplified as follows:

$$\frac{d^2r}{dt^2}=n\nabla n \tag{15}$$

Therefore, Eq. (12) can be solved numerically by the 4th order Range-Kuttab method.

$$\left\{\begin{array}{l} r_1=r_0+\frac{h}{6}(K_1+2K_2+2K_3+K_4) \\ T_1=T_0+\frac{h}{6}(L_1+2L_2+2L_3+L_4) \end{array}\right\} \tag{16}$$

where h is the selected step size; $r_0(X_0,Y_0,Z_0)$ and $T_0=n_0\nabla n(r_0)$ represent the initial position of the beam and the initial direction of propagation, respectively. Parameters K_1, L_1, K_2, L_2, K_3, L_3, K_4, L_4 are defined as follows:

$$\{K_1=T_0\ L_1=D(r_0)\ \} \tag{17}$$

$$\left\{K_2=T_0+\frac{h}{2}L_1\ L_2=D\left(r_0+\frac{h}{2}K_1\right)\right\} \tag{18}$$

$$\left\{K_3=T_0+\frac{h}{2}L_2\ L_3=D\left(r_0+\frac{h}{2}K_2\right)\right\} \tag{19}$$

$$\{K_4=T_0+hL_3L_4=D(r_0+hK_3)\} \tag{20}$$

For beams with different angles of collision between the target point and the camera's optical axis, the position r_0 in the center of the camera is fixed hypothetically, and the direction of light emission is determined according to the target point. According to the initial position of the r_0 ray and the initial direction of the T_0 ray, the beam can be traced from this point to the next location with the characteristics of r_1 and T_1. This tracking process continues until the entire tracking process is completed.

To perform the entire radiation tracking method, its refractive index and slope are required in any location in the domain and light environment. However, the outputs of the CFD calculation are discrete refractive index and distribution slopes based on the vertices of the quadrilateral grids, as described in Fig. 2. If the position of the beam is located in a quadrilateral network, for example point P in Fig. 2 or on the boundary, the inverse distance averaging interpolation algorithm was used based on a triangular mesh to obtain the refractive index and slope of the refractive index at point P. In the first step, the triangular mesh is created by DeLaney method with the help of MATLAB software with the help of primary network points. In the next step, the triangular grid and the nearest nodes marked in red are searched and determined among all points in the grid using MATLAB software. The variables n1, n2 and n3 represent the refractive index of the three vertices of the triangular lattice containing the point p.

The value of refractive index n at point P can be expressed by the weighted average of the inverse distance as follows:

$$n=n_1\varphi_1+n_2\varphi_2+n_3\varphi_3 \tag{21}$$

Where $\varphi_i(i=1,2,3)$ can be calculated as:

$$\varphi_i=\frac{\frac{1}{d_i}}{\frac{1}{d_1}+\frac{1}{d_2}+\frac{1}{d_3}}\quad(i=1,2,3) \tag{22}$$

Where $(i=1,2,3)$ di are the distances between the points p (x, y) and the points 1, 2, and 3 of the vertices of the triangular grid, which are calculated as follows.

$$d_i=\sqrt{(x-x_i)^2+(y-y_i)^2}\quad(i=1,2,3) \tag{23}$$

This process is also performed to calculate the slope of the refractive index at point P.

3. Problem definition and numerical procedure

3.1. Problem explanation

Unlike previous investigations, this study does not circumscribe itself to the area beneath the wave, and interestingly, it focuses is beyond the interaction border between air and water and more importantly on how those changes could affect the deflections, by doing a series of 2-dimensional simulations on hydrofoils with a chord length of C which is submerged at a distance of h from the free surface of the water This paper is particularized its investigation on NACA series hydrofoils with a range of thickness from 9% to 15% of cord and variations in camber the its location like NACA2409, NACA2412, and NACA2415. This variation has targeted the changes in geometrical alterations and the other parameters such as angle of attack and submerging depth, known as h/c.

The criteria of changes in the hydrofoil type are self-explanatory, but the other alterations have their limits. As a matter of fact, all hydrofoils are studied at incidence angles of 2.5°, 5°, and 7.5° degrees. Furthermore, submerged depth (h/c) varies in the range of 0.5, 0.7, and 1. In order to have efficacious results, the alterations are applied separately while other variables remain unchanged.

Solving procedure began by simulating the wave for submerged hydrofoils with ANSYS FLUENT which has got two reasons: obtaining the density field in the solution domain is the prior one, and the other one is understanding the shape of the formed wave. Then the density field is transferred into the MATLAB code, which solves the density field based on a rung-Kotta solver.

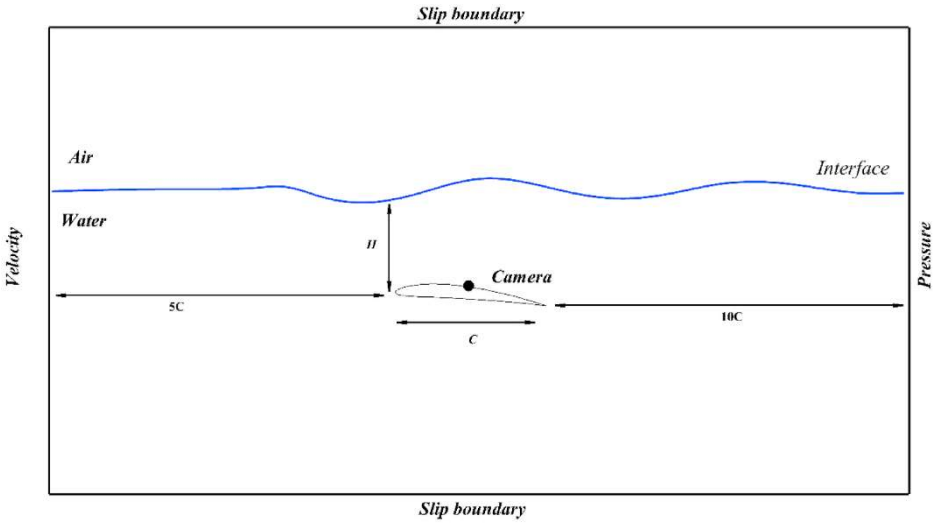

Fig. 3. Dimension and boundary conditions of the two-dimensional domain.

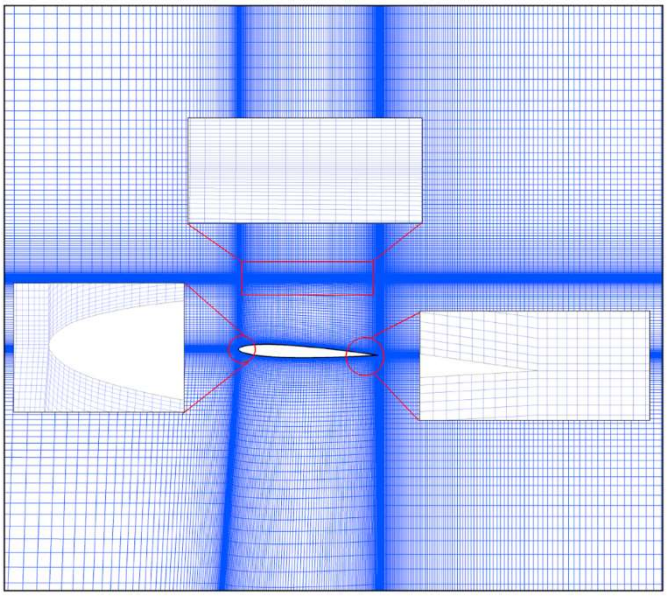

Fig. 4. Mesh resolution around hydrofoil and free surface.

Table 1
Setting of Numerical simulation.

Flow	Turbulent
Solver	2- D Double precision
Momentum equation solver	Second order upwind
Solver	Simple
Turbulent model	k-w SST

3.2. Mesh generation and solution algorithm

This paper scrutinizes a two-dimensional hydrofoil advancing to a close distance from the free surface of the water. In order to verify the solution, a simulation of flow has been performed around the hydrofoil with the NACA4409 section. As shown in Fig. 3 the left side indicates the inlet for air and water. Subsequently, the right demonstrates their outlet. The computational domain in the downstream should be large enough in order to provide a thorough velocity field in order to serve the purpose of constant velocity condition in the inlet. According to this reason a

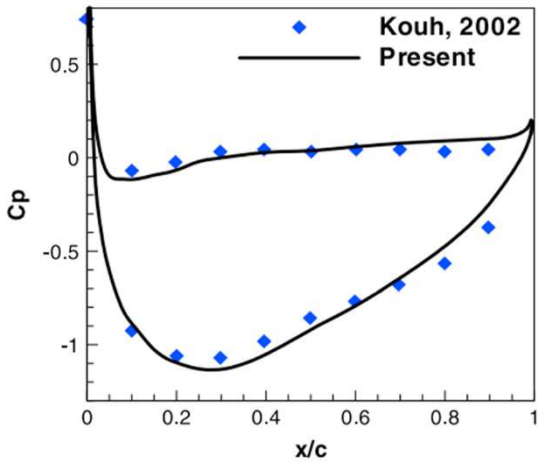

Fig. 5. Comparison of numerical and experimental pressure coefficient distribution around the NACA4412, AOA = 5, and $h/c = 1$.

distance of 5C is chosen to have a fully developed flow.While velocity is prescribed, the pressure value is considered constant, and upper and lower boundaries are assumed to have slip-type boundary conditions. In addition, the hydrofoil surface is considered no slip boundary condition as a wall boundary between the flow and the structure. Furthermore, considering the k-w SST turbulent model has an including viscosity limiter that keeps y^+ in ranges near one. Subsequentely the camera is put in the middle of the hydrofoil.

After examining several different lengths, the dimensions of the domain were chosen. In this simulation, the fully structured mesh is developed because of the H-type grid simplicity and applicability to the current flow configuration, and more importantly, in order to capture the free surface in a precise manner, this griding is utilized. Subsequently, the schematic shape of the 2D-mentioned grid is illustrated in Fig. 4.

Most contemporary pressure-based methods employ a sequential iteration technique in which the different conservation equations are solved one after another. The typical approach to enforcing continuity is taken by combining the equation for continuity with those of momentum to derive an equation for pressure or pressure correction. Moreover, solving procedure of the present investigation is by applying the SIMPLE technique in which the implicit discretized equations are solved by a sequence of predictor and corrector steps.

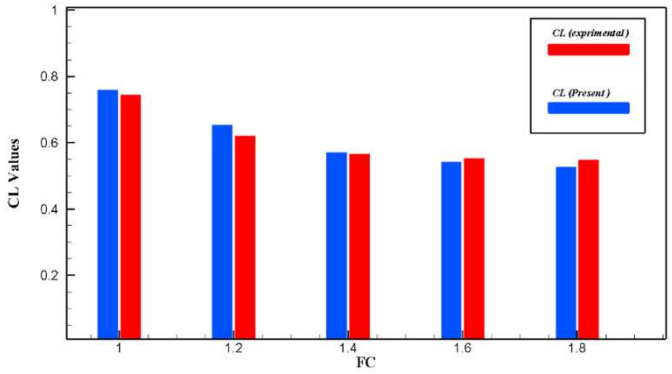

Fig. 6. Comparison of numerical and experimental lift coefficients in both numerical simulation and experimental work of (Kouh et al., n.d.).

3.3. Fluid flow validation

Selecting a fixed number of cells requires copious efforts and trials, various grid sizing is tested, and their effect on the pressure coefficient was investigated and the trend had not significantly changed after 104000 cells and consequently a grid with 84000 cells was selected as an independent one.

The setting numerical solution is explained in Table 1. When dealing with two-phase flow simulation and moving hydrofoil near the free surface of the water, the Froude number is considered according to the hydrofoil chord (Fc). To validate the simulation, Fig. 5 indicates the pressure coefficient distribution on the NACA4412 hydrofoil surfaces for an AOA $= 25$ and $h/c = 1$.

Juxtaposing numerical results with the experimental ones from (Kouh et al., n.d.) investigation demonstrates that the numerical results are highly reconcilable with the published results. Subsequently, Fig. 6 draws an analogy between the lift coefficient for the present calculation and the experimental value on the different Froude numbers. It can conclude that the numerical results are in a high-quality adaptation with experimental data. Consequently, the mesh characteristics and simulation parameters for current cases have been chosen according to this simulation.

3.4. Ray tracing method verification

Validation of the numerical method of radiation tracking used in aero-optical problems is very complicated, mainly due to the lack of valid experimental data. To evaluate the validity of the proposed method, an environment with radial rotations was considered for which there is a definite solution. The distribution of the radial refractive index is assumed to be as follows:

$$n(x,y) = n_0\sqrt{1-\alpha^2(x^2+y^2)} \tag{24}$$

Where n_0 is the refractive index in the initial and constant position a, the radial gradient distribution is the mean refractive index. The analytical solution relation can be expressed as follows:

$$\left\{\begin{array}{l} x = x_0\cos\left(\dfrac{n_0\alpha}{L_0}z\right) + \dfrac{P_0}{n_0\alpha}\sin\left(\dfrac{n_0\alpha}{L_0}z\right) \\ y = y_0\cos\left(\dfrac{n_0\alpha}{L_0}z\right) + \dfrac{q_0}{n_0\alpha}sin\left(\dfrac{n_0\alpha}{L_0}z\right) \end{array}\right\} \tag{25}$$

$$\left\{\begin{array}{l} x = x_0\cos\left(\dfrac{n_0\alpha}{L_0}z\right) \\ y = x_0\,sin\left(\dfrac{n_0\alpha}{L_0}z\right) \end{array}\right\} \tag{26}$$

where x_0 and y_0 are the point coordinates of the collision, P_0, q_0 and L_0 express the cosines of the original direction. (The result of calculating the cosine direction and refractive index). The values of these parameters were determined as $P_0 = 0, x_0 = \frac{q_0}{n_0\alpha}, y_0 = 0$.

The relative error of the radiation tracking method can be defined as follows:

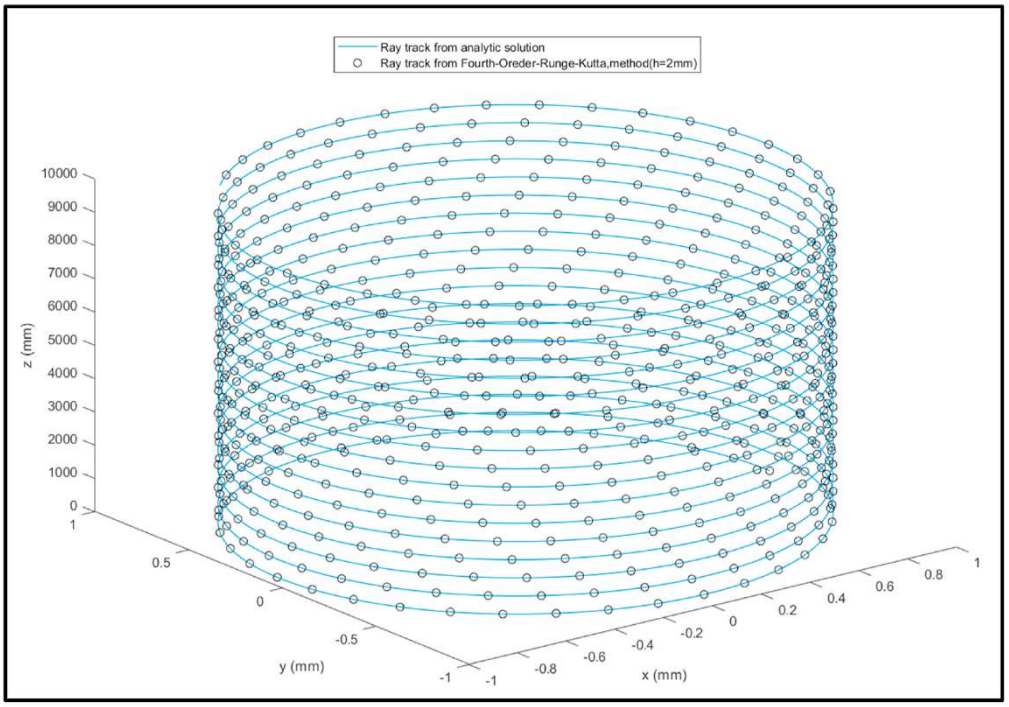

Fig. 7. A compassion between analytical results with numerical solution with 4th order Rung Kutta.

Table 2
h independency from the number of iterations.

Case	h	Iteration	Deflection
1	0.1	30	−65.571
2	0.2	15	−64.928
3	0.3	10	−66.174
5	0.5	6	−66.183
6	0.6	5	−59.652
7	0.01	300	−68.188
8	0.02	150	−67.831
9	0.03	100	−69.072
10	0.04	75	−67.731
11	0.05	60	−67.491
12	0.06	50	−67.363
13	0.001	3000	−67.960
14	0.002	1500	−68.068
15	0.003	1000	−67.920
16	0.004	750	−67.970
17	0.005	600	−67.988
18	0.006	500	−67.899
19	0.0001	30000	−67.998
20	0.0002	15000	−67.998
21	0.0003	10000	−67.991
22	0.0004	7500	−67.994
23	0.0005	6000	−68.010
24	0.0006	5000	−67.995

$$\delta(z) = \frac{|r_z - r_z'|}{|r_z|} \tag{27}$$

where r_z is the position calculated from the ray tracking method on the plane z and r is the actual position of the ray, which is from relation below. In order to validate the radiation path prediction method, refractive index parameters were determined as $n_0 = 1.5$.The initial collision angle was determined by two components, side angle 0 and altitude angle of 60° degrees. As a result, the directions of the cosines q_0, p_0 and L_0 were determined as $P_0 = n_0 \sin 0° \cos 60°$, $q_0 = n_0 \cos 0° \cos 60°, L_0 = n_0 \sin 60°$. The location of the incident point is considered $x_0 = \frac{\cos 60°}{\propto}, y_0 = 0$ *and* $z_0 = 0$.

To verify the obtained numerical results, four data were evaluated by an analytical method to validate the results of the light beam tracking solution by the quadratic Range-Kutta method. The light beam tracking results compared to the analytical solution is shown in Fig. 7 which is in a good agreement between the numerical data and analytical solution and also confirmed the accuracy of the approach. On the other hand, this comparison showed good accuracy of the numerical solution and very high accuracy of the short beam tracking solution.

Furthermore, there are numerous combinations for evaluating an answer due to having various step sizes known as h and number of iterations. As the matter of the fact the first step after extracting the density filed in the entire solution was getting the exact coordinates of the hydrofoil where the solution must take place. According to the geometry of the hydrofoil the coordinates that are considered are in the middle of the hydrofoil. A fixed view is considered for investigating this procedure and the ray which is being tracked has a length of 3 km. These lengths can be changed by a multiplication of iteration and the h indecency that can be seen in Table 2.

Computational cost is one the prior objectives that matter in the procedure a fixed number of iterations should be used for all the cases as it is obvious in Table 2. The more the number of iterations goes the more prices is the answer but the changing trend is not that significant. 3000 iterations with the step size of 0.001 fulfills the proper amount of deflection.

4. Results

Ray trajectory is prioritized for the purpose of this investigation, and there are some criteria germane to these aberrations. First of all, most of the aberrations are engendered due to the shape of the formed wave. Specific parameters can vary the wave's shape, which can be regarded as the angle of attack, the submerged depth, and the shape of the hydrofoil, which will be perused in this article.

In 1981, (Janssen, 1981) a team had researched on Snell's window on how the reflections would occur from the water as the ray ejects the water or get reflected in to the water. As it is shown in Fig. 8 there is a range that light could be seen in certain depth of water and it is highly dependent on the submerged depth and the conditions of light around the viewer.

A circle of light is surrendered by darkness; besides, some light can travel throw the water but not all. At certain angles, the rays are reflected into the water, and the only vantage point is visible within the circle. This very phenomenon is proved in this paper, too. These trajectories in 2D create a cone in 3D that makes a circle at its end, as it is

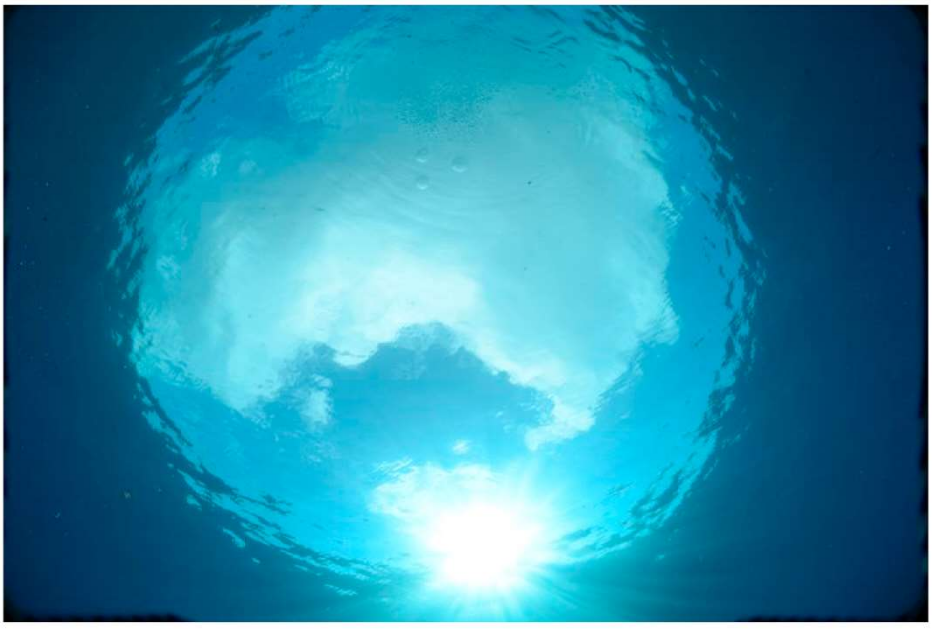

Fig. 8. Snell's window from a certain vantage point (Higton and Higton, n.d.).

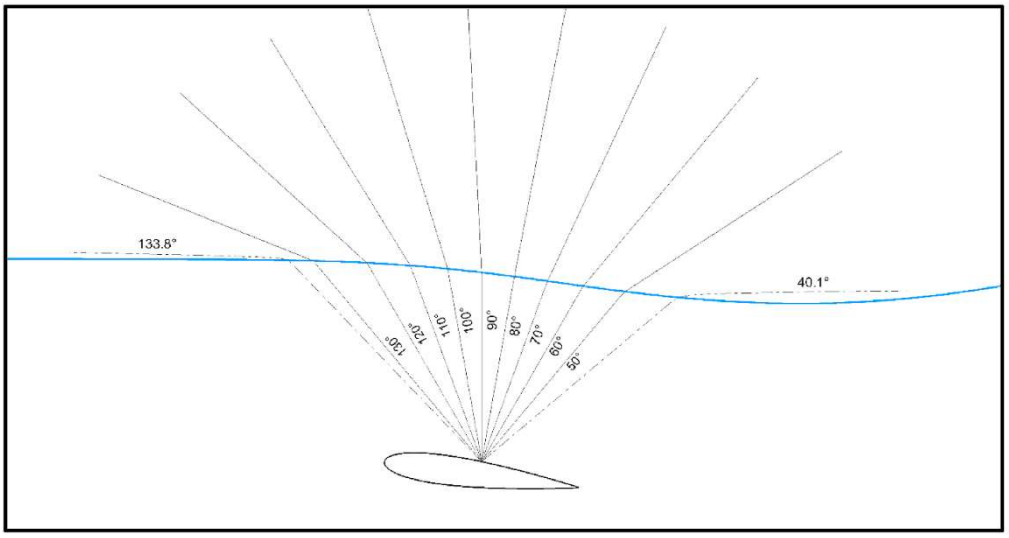

Fig. 9. Deflected rays in the range of 40.1°–133.8° degrees for NACA 0015 in $h/c = 0.5$ and AOA = 2.5°.

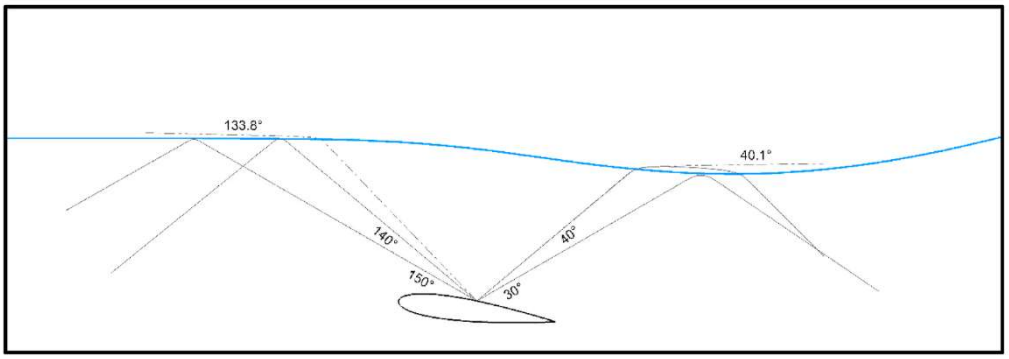

Fig. 10. Reflected rays in the range of 30°–40.1° degrees and 133.8°–150° for NACA0015 in $h/c = 0.5$ and AOA = 2.5°.

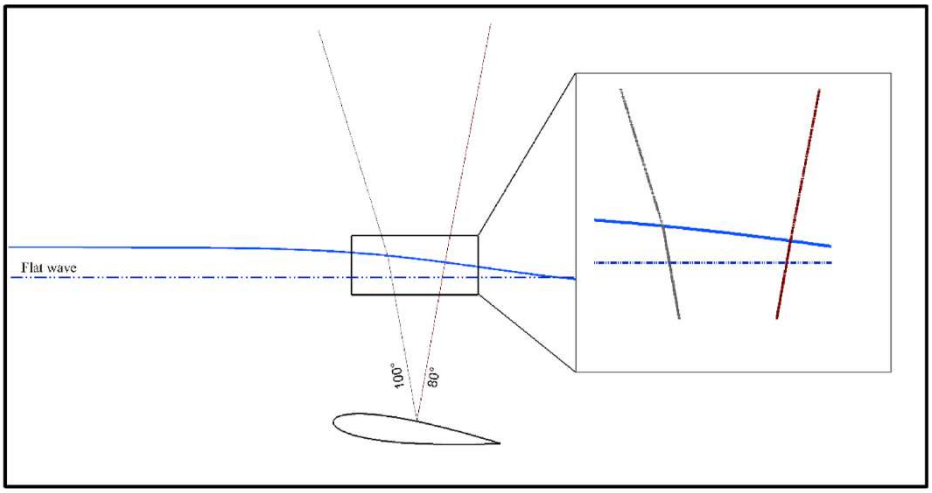

Fig. 11. NACA 0015 in $h/c = 1$, and AOA = 7.5° comparison of the ray emission in two different camera angles 80° and 100°.

shown in Fig. 8. There is an eyesight limitation caused by the same window, which is in the form of a circle.

To be more acquainted with the procedure of the ray-tracing approach and its dominance on Snell's window, the hydrofoil NACA 0015 is chosen at submergence depth of $h/c = 0.5$ and AOA = 2.5° as iullstrated in Fig. 9, and Fig. 10. Interestingly enough, the window can be observed between the angles of 40.1° and 133.8°, and this information would espouse Snell's window. Moreover, the area between these two angles is known as the eyesight limit, and any angles lower than 40.1° and higher than 133.8° would aggravate the sight and give an obscure image from the area in the bottom.

According to **these two last figures**, ray angles set the eyesight

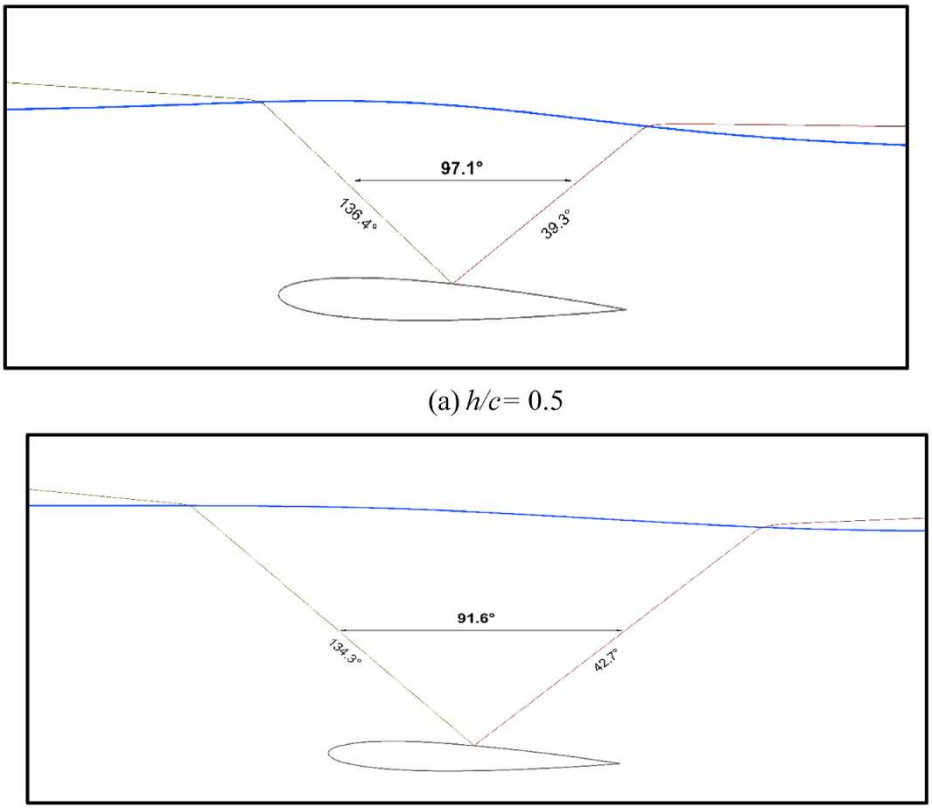

Fig. 12. NACA 0012 hydrofoils in a AOA = 2.5°vundergoing different submergence depths.

Table 3
Critical angles behind and Infront of the camera.

h/c	Critical Angle behind the camera	Critical Angle Infront of the camera	Window's angle
0.5	39.3°	136.4°	97.1°
0.7	40.8°	135.5°	94.7°
1	42.7°	134.3°	91.6°

restrictions that other rays rather penetrate the water or reflect into it. This phenomenon is known as the critical angle. Furthermore, it could be denoted that none of those deflections are tantamount to one another other, and they have got their particular value due to their angle with the surface of the water.

Unambiguously, the amount of deflections in case of having a flat surface of the water can be more distinguishable than when it is not. Likewise, when the ray is emitted perpendicularly to the water's surface, there is no deflection in its trajectory, and as it gets further from 90°, its deflection tends to be more severe. Additionally, there is a perfect symmetry in the ray's track before and after the undeflected ray. This generalization espouses the minor and negligible deflections that occur when the camera angles are set between 80° and 90°, but the wave's shape causes different impact angle approximately perpendicular to the surface. At one time, the wave's form is one of the particular foundations of all deflections. Although previous investigations prove asymmetry in deflections on flat surfaces of the water, this notion is not particularly corroborated in this investigation. Two symmetrical rays tracing angles with values equal to 80° and 100° are nominated to authenticate this specific contrast. As illustrated in Fig. 11 unlike the expectations manifest, similar deflection is not reached, it is clear that the outcomes contradict one another, and the amount of deflections are in the first case that is observing the area behind with angle of 80° and the front sight for the angle of 100° are, 1.488°,and 4.433° respectively, which proves that the deflection variation is approximately triple.

This differentiation is merely contingent upon the wave's shape, which indicates the place of impact. As it has already been stated, if the ray had been closer to the perpendicular zone, it would not have undergone any deflections. So closer collision to a perpendicular zone encounter less severe deflections. The contact angle for the camera angle of 80° is about 78° and for 100° is about 72°. Consequently, this 6° difference causes the triple amount of deflection.

Undeniably this particular case is not able to singly handed clarify the number of deflections for all those cases, so there are copious comparisons for more convenient elucidations.

4.1. Effect of submerged depth

One of the most vital factors that lead to specific changes in Snell's window is the submerged depth; in fact, changing the submerged conditions can affect the formed wave, and the wave itself is a prior parameter to the Snell's window. The illustrated hydrofoil in Fig. 12 is NACA 0012 in a constant angle of attack as 2.5° and the only parameter that varies in this part of the research is the depth *(h/c)* which changes from 0.5 to 0.7, then 1. More obscure sight is gained by being in deeper water.

Table 3 demonstrates the critical angles in which the ray won't either penetrate the water or deflect into it. Although as the hydrofoil experiences deeper submerging depth, the critical angle increases behind the camera and decreases in front of it and the window gets narrower for 3.25% in the first level of alteration; then, it diminishes for another 3.38% when submerge distance *(h/c)* changes from 0.7 to 1. The window's width is shown in Fig. 12.

According to Fig. 12. It is evident that the wave's form tends to falter

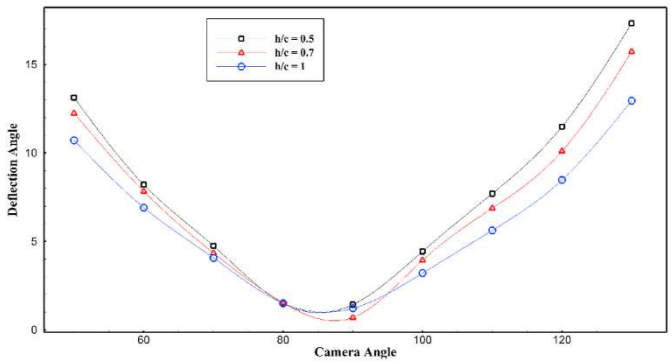

Fig. 13. The amount deflection for NACA 0012 in AOA = 2.5° and different h/c in various camera angles.

as the hydrofoil is immersed in a deeper spot. Although the Snell's window gets more attenuated, the amount of deflections will indeed be less than in the other cases.

To get a better view on how the changes occur in different camera angles and different submereging depth, they have been collected and demonstrated in Fig. 13.

Fig. 13 is drawn in the range of the snell's window and can clarify the manner of alterations, the amount of deflection changes between the maximum value of 17.2° and minimum values close to zero. On the one hand, the deflection trend is approximately firm thorough the alterations, and as the hydrofoil is submerged in shallower water, the deflections tend to be more severe. On the other hand, the only spot contradicting the variation of trend is when the camera angle is set between (80° and 90°) which would cause a perpendicularity between the ray and the water's surface.

In order to expound the ray's adjustment in various submerging depth two arbitary cases are selected. In accoradnce with Fig. 14. NACA 0012 hydrofoil is utilized and its equivalent submeregence depths *(h/c)* are 0.5 and 0.7 and a fixed AOA equal to 2.5°.

Accoring to Fig. 14. Changes in surface curvature are somehow tantamount to one another, and they elucidate that this alteration is not merely due to the wave's curvature and is related to the submerging depth. More on that, a falt surface would have gone through these deflection paterns and when the ray length increases in the water zone due to the submergence depth.

Even though the camera is fixed in the middle of the hydrofoil and neither the shape of the hydrofoil nor the angle of attack changes across the investigation, there are certain alterations in the amount of the deflection in different cases, which leads us to the conclusion that the amount of depth is the main reason of changes in the form of the wave. Moreover, without a doubt, pressure is one of the critical features that alternates the wave shape. There are two kinds of applied pressure: hydrostatic and hydrodynamic. Dynamic pressure is the kinetic energy per unit volume of a fluid and is one of the terms of Bernoulli's equation, which can be derived from the conservation of energy for a fluid in motion. Subsequently, it appears as a term in the incompressible Navier-Stokes equation. More precisely, the dynamic pressure equals the difference between the total and static pressure.

When the hydrofoil experiences higher velocities, the dynamic pressure consequently increases. Fig. 15 demonstrates the dynamic pressure field around the hydrofoil for two submerge distances (h/c = 0.5 and 1). Also, Fig. 16 depicts the streamwise velocity in the same condition. Passing the flow between the upper bump of the hydrofoil and the free surface can be modeled as a flow in a converged-diverged nozzle, and the velocity increases and drops at the trailing edge of the hydrofoil. Therefore, Fig. 15 indicates growth in dynamic pressure, specifically on the hydrofoil's bump, and reduces at the end of the hydrofoil. On the other hand, this velocity alteration affects the free surface and forms a wave.

According to Bernoulli's law, the relation between pressure and velocity is contrary. Consequently, an increase in the amount of hydrodynamic pressure leads to an increase in the amount of velocity. The previous figure shows that the hydrodynamic pressure distribution sets the wave's geometry. These changes in pressure lead to changes in velocity filed, as demonstrated in Figs. 15 and 16.

As Figs. 15 and 16 clearly demonstrate, either the dynamic pressure and velocity are zero on the tip of the leading edge of the hydrofoil but interestingly, the overgoing flow's velocity tends to increase on the top of the hydrofoil which consequently follows this the in the dynamic pressure. As the flow goes towards the leading edge, its velocity diminishes and moderates the dynamic pressure. Furthermore, Table 4 illustrates this significant decrease. For instance, in h/c = 0.7,by checking two points on near 20% of C and the other near 80% of C outcomes 39.14% drop in the dynamic pressure, resulting from the 21.98% lessening in its velocity. These alterations are the reason for the

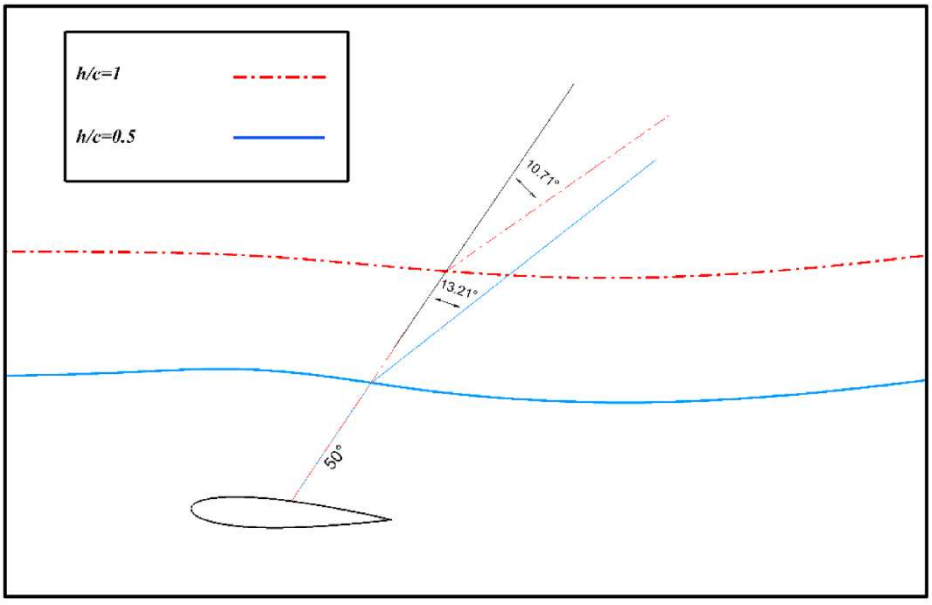

Fig. 14. Comparison of the ray emission for NACA 0012 in AOA = 2.5° in a fixed camera angle that is 50° in two different h/c which is 0.5 and 1 respectively.

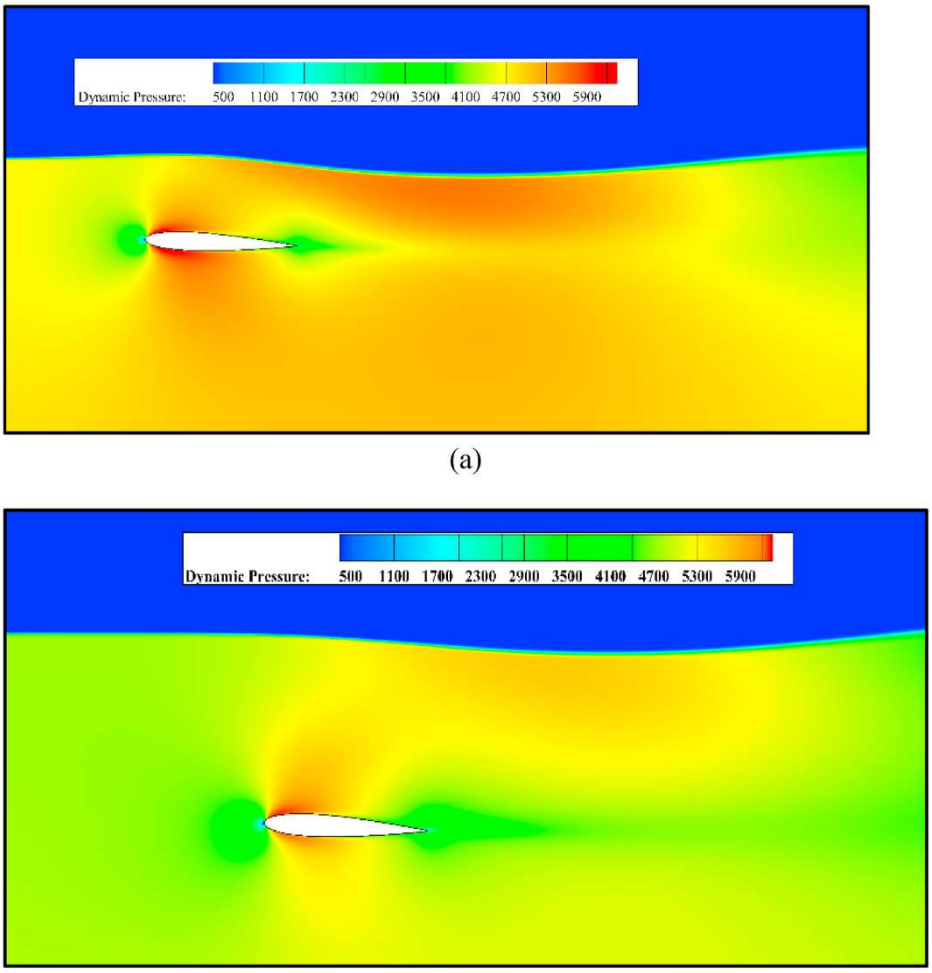

Fig. 15. Pressure per (Pa) contours on NACA 0012 in AOA = 2.5, in different submerging depth as a) $h/c = 0.5$, and b) $h/c = 1$.

varied waves formed in different h/c. As disscused before this growth in velocity ends up to a decrease in pressure (according to Bernoulli's law) which sucks the water's surface towards the hydrofoil creating the formed waves.

4.2. Effect of attack angle

Changing the incidence angle can modify the formed wave, and as previously proved, the wave itself is a prior parameter to Snell's window. NACA 0009 hydrofoil is chosen in a submergence depth *(h/c)* equal to 0.5, and by having increments in the angle of attack, the window opens to a broader scale. In order to justify the claim, Table 5 is illustrated to set the eyesight boundaries by identifying the camera's critical angles, which depicts Snell's window width.

As is demonstrated in Table 5, Although by increasing the AOA, the critical angle tends to decrease on the front side of the camera, and interestingly enough, the trend contradicts on the opposite side, this would eventually lead to an enlargement in Snell's window width for 1.57% and 2.12% by doubling and tripling the AOA respectively. It has to be kept in mind that all these changes are highly dependent on the form of the wave since the ray length in the water zone was approximately considered a constant value. Even though the camera's position is fixed in the middle of the hydrofoil, the angle of attack variation will slightly change its spot. The absolute ray length in water zone alterations is shown in Table 5. It is clear that when the hydrofoil's angles get doubled, the depth increases by 7.5%, and subsequently, for a triple value, the growth is 11.2%. As previously concluded, the ray length in the water zone was correspondingly a vital parameter on Snell's window that raised the expectation to observe the tantamount result in this case as well.

According to Fig. 14, it was proved that when the hydrofoil is submerged in deeper areas, the deflections get less in comparison to the previous state, but in order to elucidate the cause of deflection, NACA 0009 is chosen in $h/c = 0.5$ to proclaim the length of ray in water zone for various AOAs in a constant camera angle of 50°. Moreover, the deflection trend is indicated in Fig. 17, and the ray-length variations for this particular case are demonstrated in Table 6.

According to Fig. 17, a referencing line with angle of 50° is drawn and the amount of deflection for each particular case is separately shown with the value of Θ, despite the minor escalation in ray length, these severe changes in deflection amount are surprising cause the changes in both cases are analogous, while the changes in ray length are excessively incompatible in comparison with the case in Fig. 14. Thus, the merely feasible deduction would be the change of the wave's shape, not the ray length. Displacements in the camera's point of view end up with a different impact placed on the water's surface. More importantly, the surface level and shape change due to AOA variations, which is illustrated in Fig. 18.

According to Fig. 18, the wave's shape alternates in the front and beyond camera's area. So, coming to a symmetrical result is equivocal. In order to clear the obscurity the same case in pervious part with the symmetrical camera angle (130°) is investigated and the following

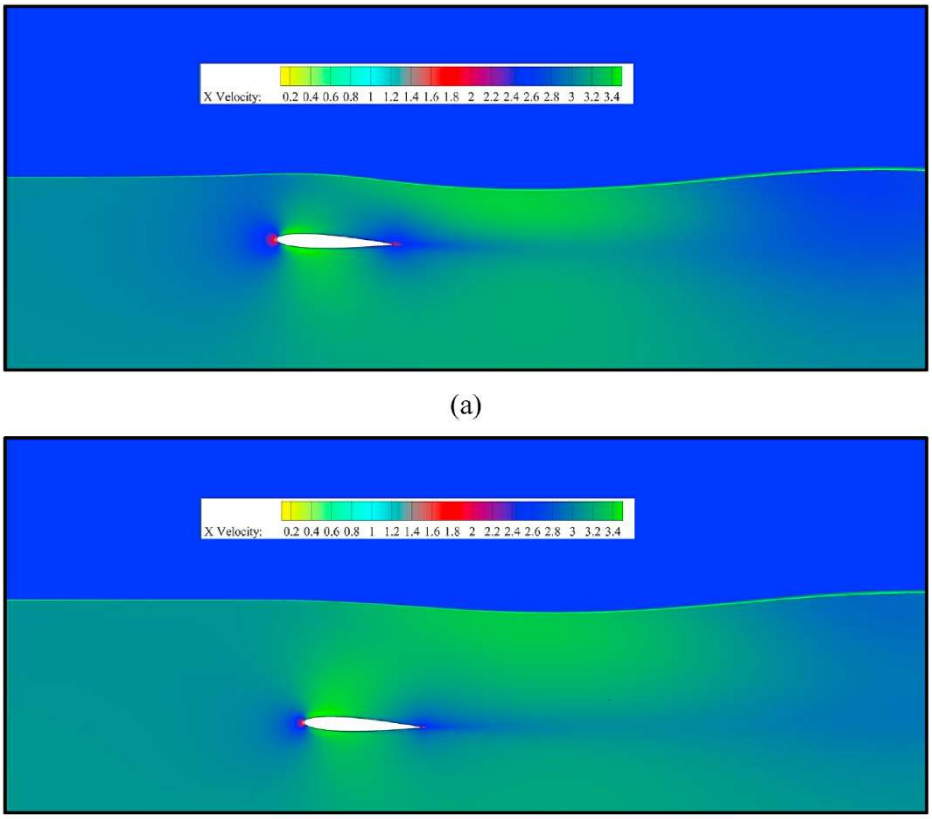

Fig. 16. Velocity (m/s) contours on NACA 0012 in AOA = 2.5, in different submerging depth as a) $h/c = 0.5$, and b) $h/c = 1$.

Table 4
Dynamic pressure and velocity on the 20% and 80% of the hydrofoils cord for NACA 0012 in AOA = 2.5° and various h/c.

h/c	Dynamic pressure (Pa) on 20% C	Dynamic pressure (Pa) on 80% C	Velocity (m/s) on 20% C	Velocity (m/s) on 80% C
0.5	*5232.78*	*3166.23*	*3.235*	*2.516*
0.7	*5276.08*	*3210.95*	*3.248*	*2.534*
1	*5501.28*	*3276.59*	*3.317*	*2.559*

Table 5
Critical angles behind and Infront of the camera.

AOA	Critical Angle behind the camera	Critical Angle Infront of the camera	Window's angle
2.5°	40°	135°	*95°*
5°	38°	134.5°	*96.5°*
7.5°	36.8°	133.8°	*97°*

results are as shown in Fig. 19.

According to Fig. 19, similarly the symmetrical angle is studied but, unlike in the last section unidentical outcome is reached in areas behind and in front of the camera. As previously proved, this is merely due to the wave's shape. As the wave's shape is flatter in the front area, the impact point will be closer to 90°, and consequently, less deflection will be detected. Under this particular case, as the AOA reaches 5°, deflection increases by about 9%, and subsequently, after reaching 7.5°, its deflection rises by 14.33% in juxtaposition with the first case with AOA = 2.5°.

This contradiction would motivate the analysis of the changes for all cases to adjust a trend for these variations. All camera angles are investigated per different AOAs, and consequently, Fig. 20 is

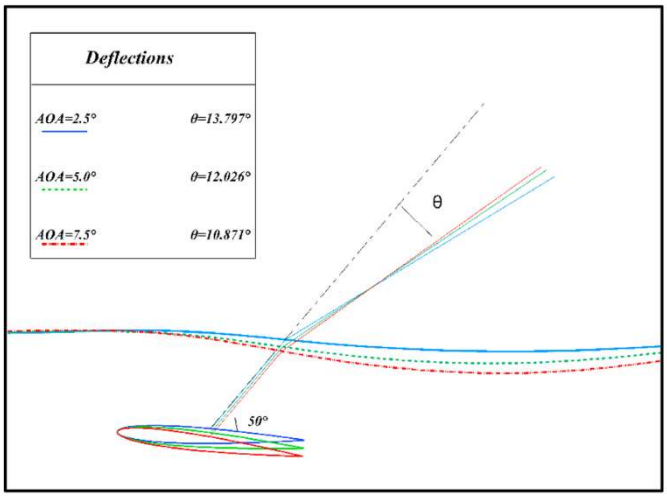

Fig. 17. Ray deflections for NACA 0009 in approximately constant h/c of 0.5 and various AOAs for camera angle equal to 50°.

Table 6
Depth alterations due to AOA variations.

AOA	2.5°	5°	7.5°
Ray length (m)	0.466	0.504	0.525

engendered.

Interestingly enough, as Fig. 20, shows, The previous hypothesis turns out to be feasible. As the hydrofoil perceives the area beyond the

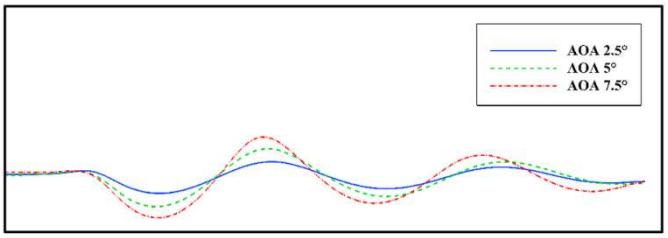

Fig. 18. Wave shape variation due to the alterations of the angle of attack.

deflection trend seems to be more severe at the lower angle of attack, the maximum deflection value is about 22.6° which occurs at AOA = 2.5°, and other AOAs have that maximum commensurate value at camera angle in the position of 40°. Furthermore, the deflection reduction trend is sustainable until the angle is approximately perpendicular to the wave's surface. However, after that range, the trend completely changes, and more deflections are observed in more AOAs which confirms that the maximum deflection before the critical angle is equal to 20.14° at the camera angle of 130° at AOA = 7.5°.

These debates are on the wave's shape, drawn in Fig. 18. As formerly validated, the wave will specify the ray's impact position on the water's surface. The pressure alteration causes these surface-level deviations, and dynamic pressure which circumscribes the wave's alteration range was hitherto investigated. Presently, the pressure coefficient on a hydrofoil is investigated and illustrated in Fig. 21. Therefore, growth in AOA decreases the pressure on the hydrofoil's leading edge, generates a suction side on the top of the hydrofoil and sucks the water's surface towards the hydrofoil, and procreates a wave with higher height and length, as is shown in Fig. 18.

4.3. Effect of Hydrofoil's geometry

The previous sections were about changing the condition of the hydrofoil, but the hydrofoil's geometry can play a vital role in forming the wave and, consequently, the size of the Snell's window, which is the direct function of the submerged object's vision from the up above. Investigating both thickness and camber effect would be absture and would confound the matter, so three hydrofoils sharing the same conditions of the immerse depth of $(h/c) = 1$ and AOA = 7.5° are chosen with distinctive varying geometry parameters.

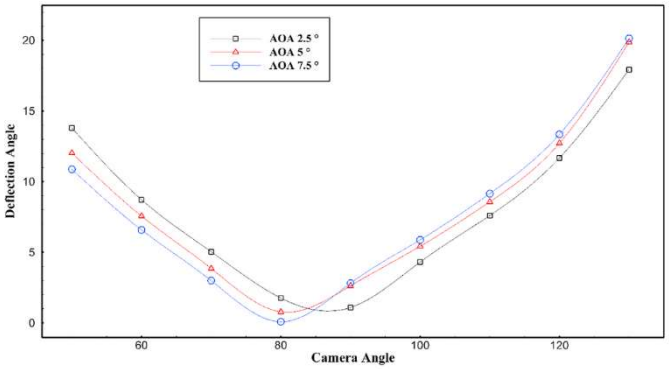

Fig. 20. Deflection amount for NACA 0009 in $h/c = 0.5$ and different AOAs in various camera angles.

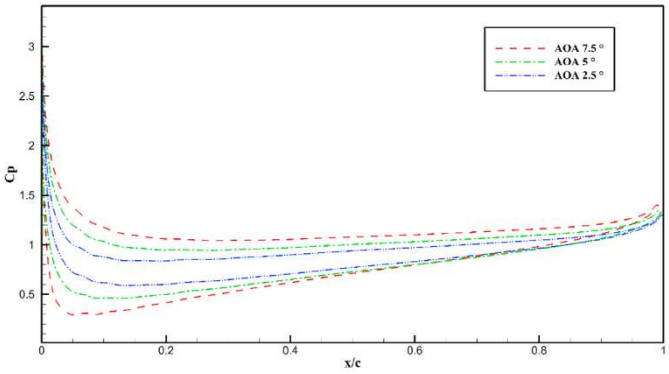

Fig. 21. Pressure coefficient on hydrofoil in different angles of attack.

Table 7
Critical angles behind and Infront of the camera.

Hydrofoil Thickness ratio	Critical Angle behind the camera	Critical Angle Infront of the camera	Window's angle
9%	40.8°	133.2°	92.4°
12%	40.5°	133.3°	92.8°
15%	40.1°	133.8°	93.7°

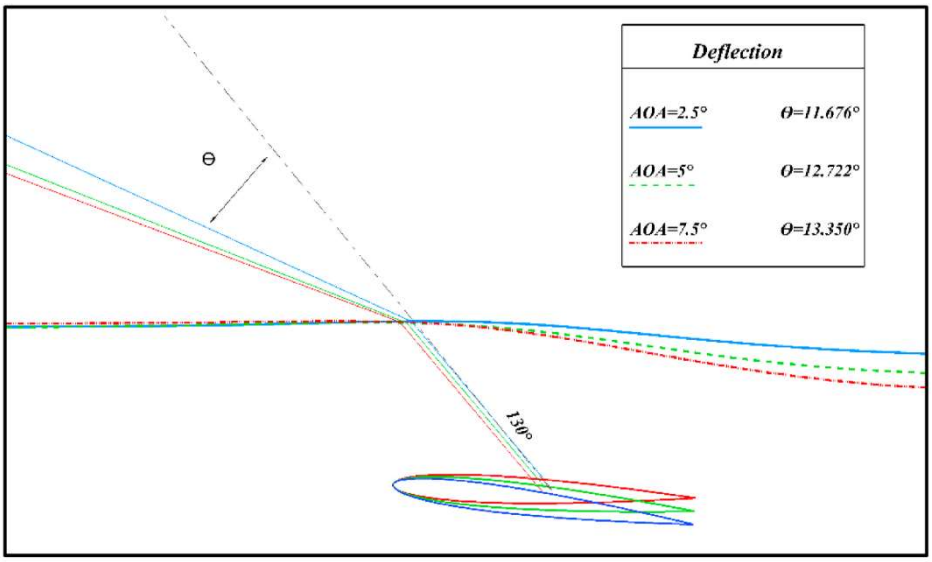

Fig. 19. Ray deflections for NACA 0009 in approximately constant h/c and various AOAs with a constant camera angles = 130°.

Table 8
Depth alterations due to Thickness variations.

NACA series	0009	0012	0015
Ray length (m)	1.0256	1.0122	0.9987

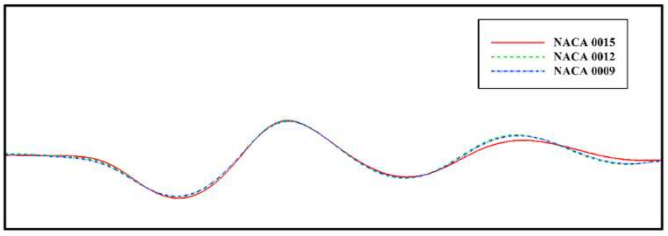

Fig. 22. Wave alteration due to changing hydrofoil's thickness for NACA 0009, NACA 0012 and NACA 0015 in $h/c = 1$ and AOA $= 7.5°$.

4.3.1. *Effect of Hydrofoil's thickness*

Firstly, in order to merely investigate the thickness effect hydrofoils with no camber are selected and the amount of thickness varies from 9% t/c to 12% t/c and finally 15% t/c. One reasonable way to obsereve the

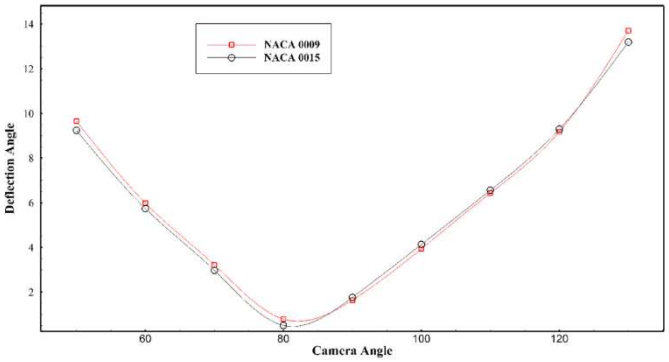

Fig. 25. The amount deflection for NACA 0009 and NACA 0015 in AOA $= 7.5°$ and different $h/c = 1$ in various camera angles.

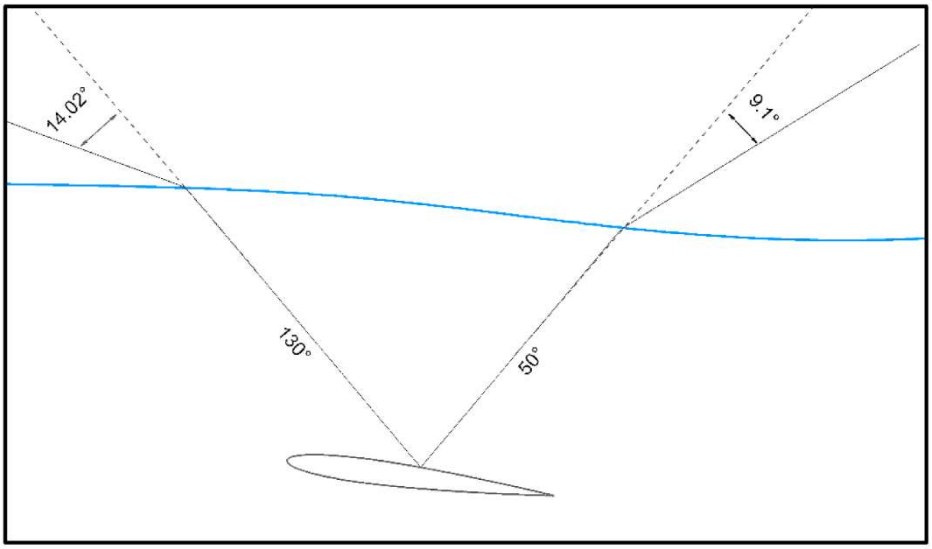

Fig. 23. Ray deflection due to changing hydrofoil's camber for NACA 0009 in $h/c = 1$ and AOA $= 7.5°$ in a symmetry camera angle.

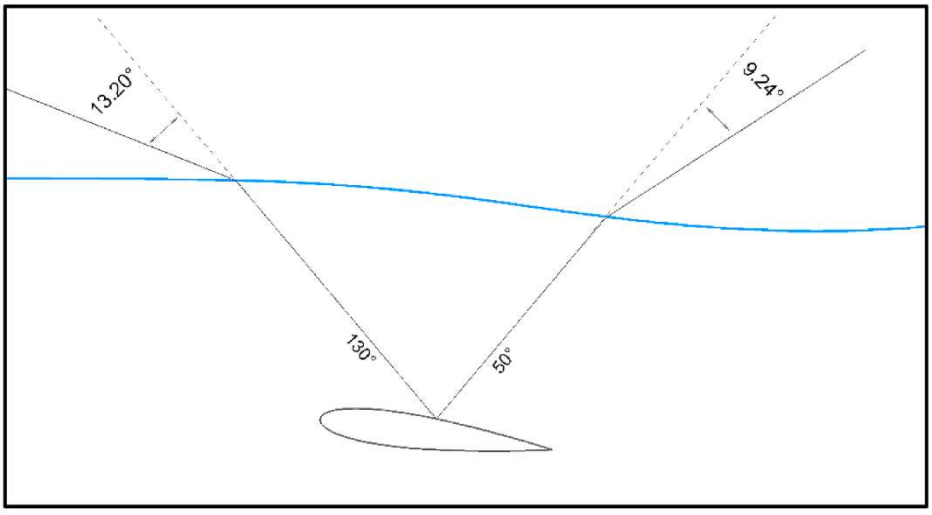

Fig. 24. Ray deflection due to changing hydrofoil's camber for NACA 0015 in $h/c = 1$ and AOA $= 7.5°$ in a symmetry camera angle.

Table 9
Critical angles behind and Infront of the camera.

Hydrofoil NACA seires	Critical Angle behind the camera	Critical Angle Infront of the camera	Window's angle
0015	40.1°	133.8°	93.7°
2415	38.5°	133.4°	*94.9°*
4415	37.1°	133.1°	96°

Table 10
Depth alterations due to camber variations.

NACA series	0015	2415	4415
Ray length (m)	0.9987	0.9788	0.9580

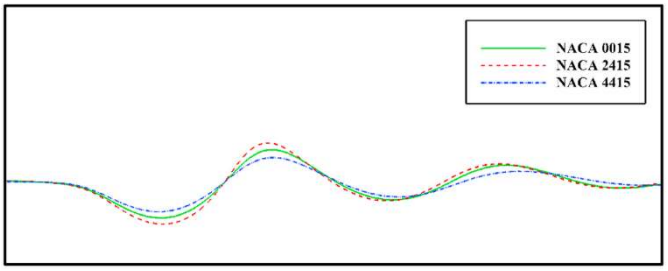

Fig. 26. Wave alteration due to changing hydrofoil's camber for NACA 0015, NACA 2415 and NACA 4415 in $h/c = 1$ and AOA = 7.5°.

effect is its dominance on Snell's window which is shown in Table 7.

According to Table 7. The broadening of Snell's window is negligible and increases by 0.4% and 1.4% from the ratio of *9% t/c to 12% t/c and 9% t/c* to *15% t/c*, respectively. As expected, two fundamental parameters can alter the amount of deflection, ray length, and the formed wave, both individually shown in Table 8 and Fig. 22.

There is approximately no alteration in the form of the wave due to the growth in thickness, as shown in Fig. 22, but that minor decrease in ray length could have altered the snell's window width. Afterwards the other important factor to be investigated is the variation of deflection and its pattern. To comprehend the trend better, the conditions of $h/c = 1$ and AOA = 7.5° are applied on the hydrofoils with *9% t/c* and *15% t/c*.

As both Figs. 23 and 24 reveal, the amount of deflections do not significantly fluctuate. By having that said, the amount of deflection in the area behind the camera increases by 15% when the hydrofoil gets 6% thicker, and in contrast, this growth in thickness causes a 5% reduction of deflection in the front area of the camera. It is noteworthy to investigate the idea that this trend is accordant with all camera angles to verify the claim that all deflection angles are shown in Fig. 25.

According to the demonstrated results in Fig. 25, the deflection alteration is not a lot, and it is somehow indistinguishable. However, the fascinating point is that deflections tend to be higher when the wave's surface tends to be falter, and thinner hydrofoil faces more deflections in the area beyond, while thicker one has got this disadvantage in the area in front.

4.3.2. *Effect of Hydrofoil's camber*

Secondly, for one more time, all the parameters are considered constant, including the thickness, but the enlarging of the camber and observing its influence on Snell's window, which is shown in Table 9.

While the pervious outcome misconstrue us to spurious conclusion that the geometrical parameter's effects are insignificant, Table 9 results are antithetical to the pervious consumption. Although the widening of Snell's window is not significant, its fluctuation is higher than altering thickness. Considering the case with no camber and then increasing camber by 2% in the same thickness expands the window by 1.3%, and even if this rise in camber is taken as 4%, the expansion in the window's width is 2.45%. Although the camera's place will be escalated as the camber climbs, its growth is not that remarkable, as shown in Table 10.

Finally the only anticipatable scenario is inspecting the camber ascendency on the formed wave, which is illustrated in Fig. 26.

Despite that the wave's form has changed for a different amount of camber, the amount of deflection does not notably alter. 4% increase in camber has increased the deflection by 21.7% in the area beyond and has decreased by 8.1% in the front area.

As the parameters have not varied since the last part, the trend will illustrate the same results but in different values, which is espoused in Fig. 27, and Fig. 28.

Applying camber on a hydrofoil will be comparable to using a hub that would generate a higher altitude wave and consequently alter the deflections in certain camera angles. These camera deflections are investigated and illustrated in Fig. 29.

According to these Fig. 29, applying camber to hydrofoil can be advantageous to some extent. Firstly, it can widen Snell's window for a better sight. Secondly, its deflections in the beyond area are less compared to the case where no camber is applied, or the camber is in lower quantity. Finally, the mere downside of having more camber is the

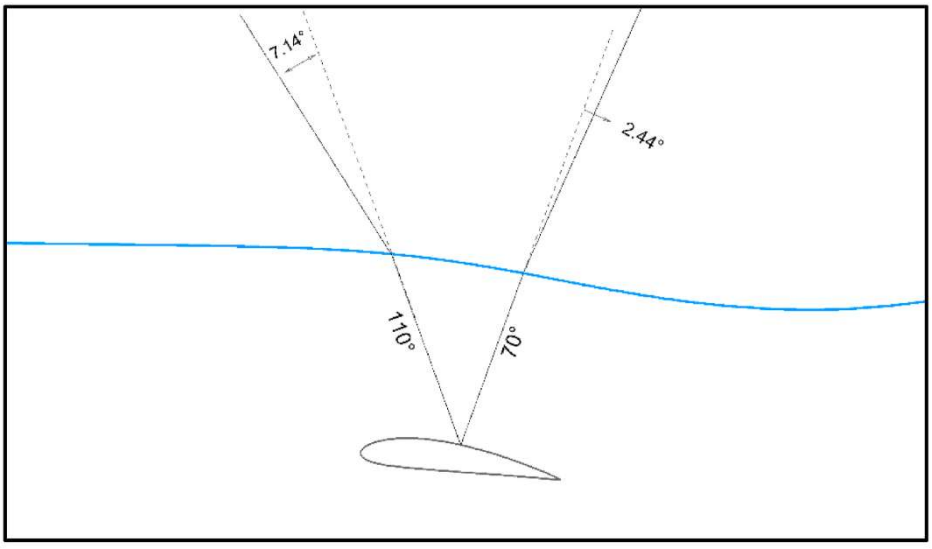

Fig. 27. Ray deflection due to changing hydrofoil's camber for NACA 4415 in $h/c = 1$ and AOA = 7.5° in a symmetry camera angle.

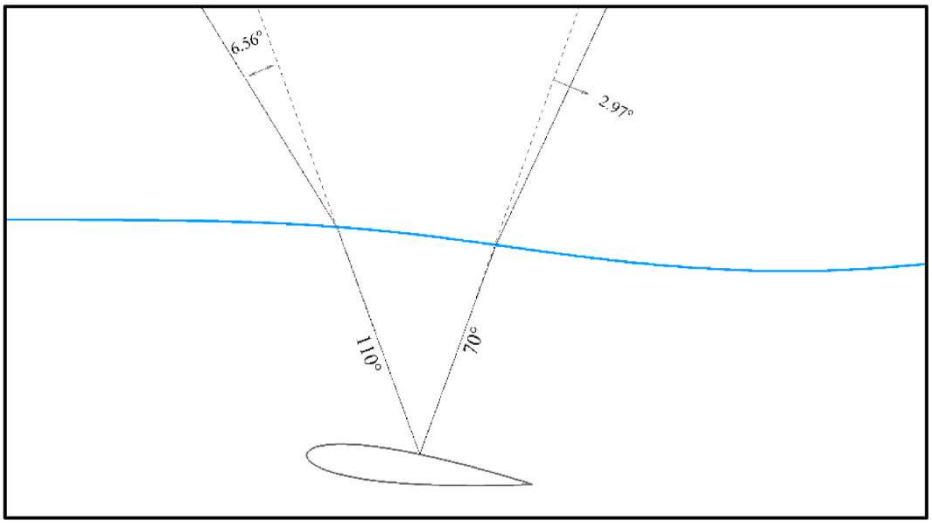

Fig. 28. Ray deflection due to changing hydrofoil's camber for NACA 0015 in $h/c = 1$ and AOA $= 7.5°$ in a symmetry camera angle.

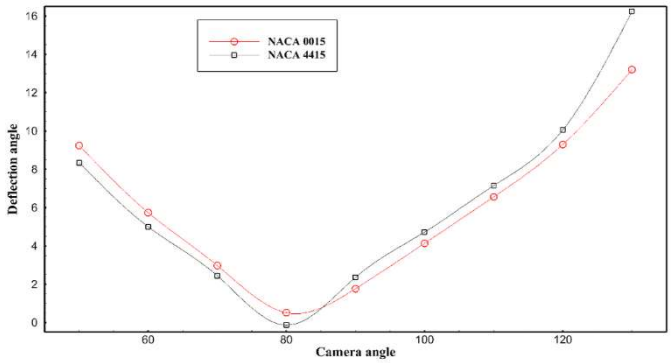

Fig. 29. The amount deflection for NACA 0015 and NACA 4415 in AOA $= 7.5°$ and different $h/c = 1$ in various camera angles.

more vague picture in the front area due to more deflected rays.

4.4. Effect of froude number

There is a ratio between inertial and gravitational forces called the Froude number. Waves, sand bedforms, and flow/depth interactions between boulders are measured with the Froude number which this study intends to investigate the Froude number's effect on the wave's shape and how it reflects on the trajectories.

For the interduced permiss a submerged hydrofoil (NACA 4412) in $h/c = 1$ and AOA $= 5°$ is chosen with a reference Froude number of 1 and is illustrated in Fig. 30.

As is demonstrated in Fig. 30, Snell window starts with 38.9°–133.4°

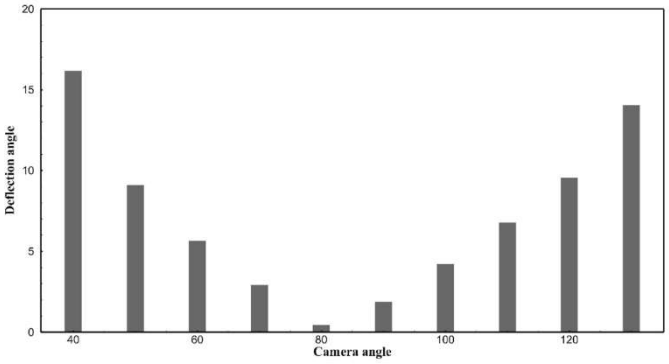

Fig. 31. Deflection trend for NACA 4412 in $h/c = 1$ and AOA $= 5°$ for the Froude number $= 1$.

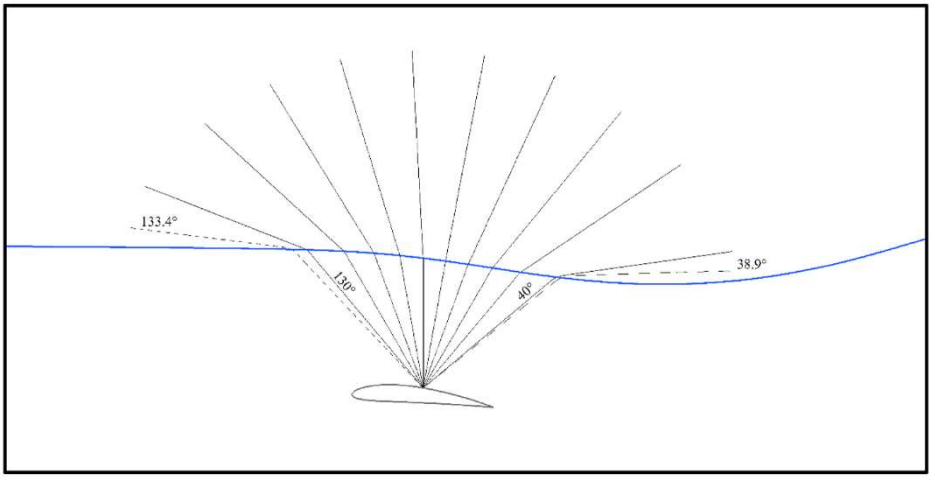

Fig. 30. Snell's window for NACA 4412 in $h/c = 1$ and AOA $= 5°$ for the Froude number $= 1$.

Table 11
Critical angles behind and Infront of the camera.

Froude number	Critical Angle behind the camera	Critical Angle Infront of the camera	Window's angle
0.4	48.1°	132.6°	84.5°
0.6	46.4°	132.8°	*86.4°*
0.8	42.5°	133.4°	90.7°

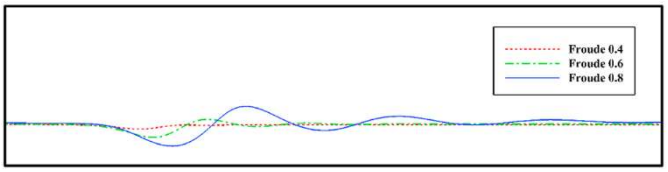

Fig. 32. Wave's shape for NACA 4412 in $h/c = 1$ and AOA $= 5°$ for various Froude number equal 0.8, 0.6, and 0.4.

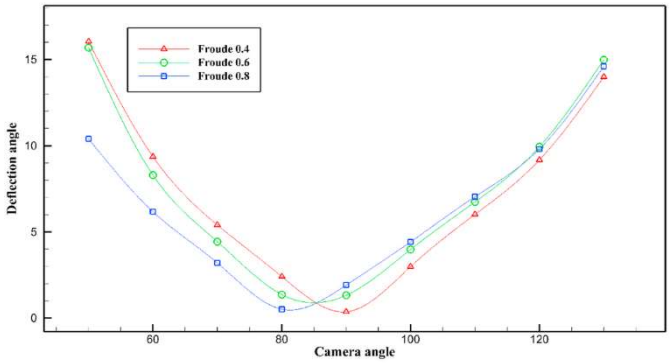

Fig. 33. The amount deflection for NACA 4412 in AOA $= 5°$ and $h/c = 1$ in different sub-critical Froude numbers for various camera angles.

Table 12
Critical angles behind and Infront of the camera.

Froude number	Critical Angle behind the camera	Critical Angle Infront of the camera	Window's angle
1.2	36.7°	135.5°	98.8°
1.4	37.5°	134.5°	*97°*
1.6	37.7°	134.1°	96.4°

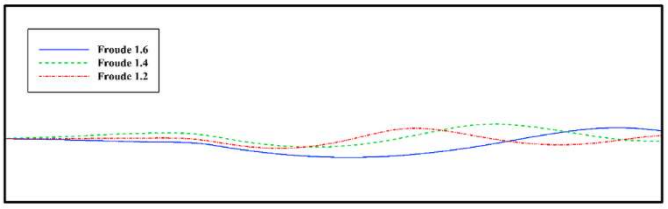

Fig. 34. Wave's shape for NACA 4412 in $h/c = 1$ and AOA $= 5°$ for various Froude number equal 1.2, 1.4, and 1.6.

and the other rays are illustrated from 40° to 130° with 10° steps. Additionally, the achieved sight is 94.5° and the defelction trend is shown in Fig. 31.

As the camera angle increases toward perpendicularity, the deflection trend plummets in all cases. In order to gain a better understanding of these trends, the subcritical and supercritical Froude numbers will be juxtaposed.

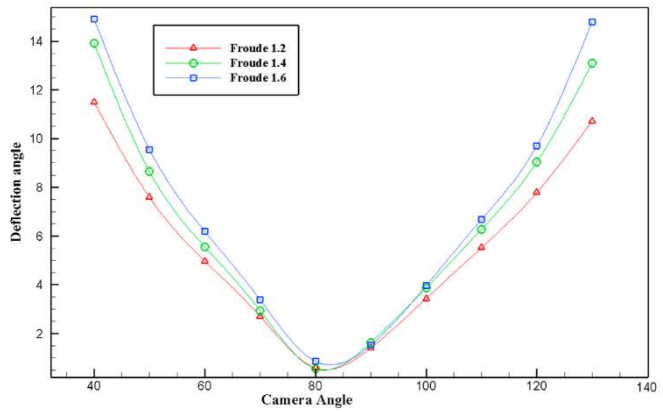

Fig. 35. The amount deflection for NACA 4412 in AOA $= 5°$ and $h/c = 1$ in different super-critical Froude numbers for various camera angles.

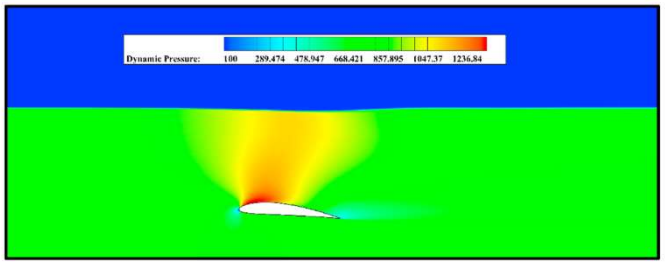

(a)

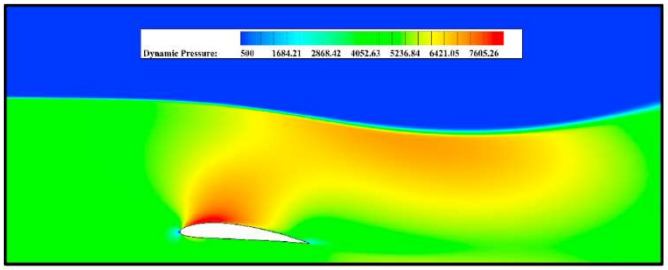

(b)

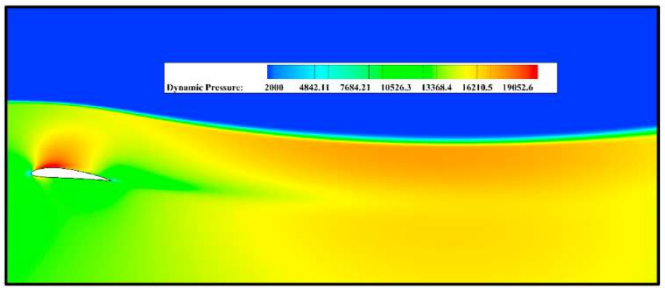

(c)

Fig. 36. Pressure per (Pa) contours on NACA 4412 in AOA $= 5$, $h/c = 1$ in different Froude numbers as a) $F = 0.4$, b) $F = 1$, and c) $F = 1.6$.

4.4.1. *Sub-critical froude number*

When the Froude number is in values below one the flow is known as the sub-critical one. This phenomenon can have an effect on the wave's shape which consequently change the Snell's window and the form of deflections. Primiraly the Snell's wnidow is shown in Table 11.

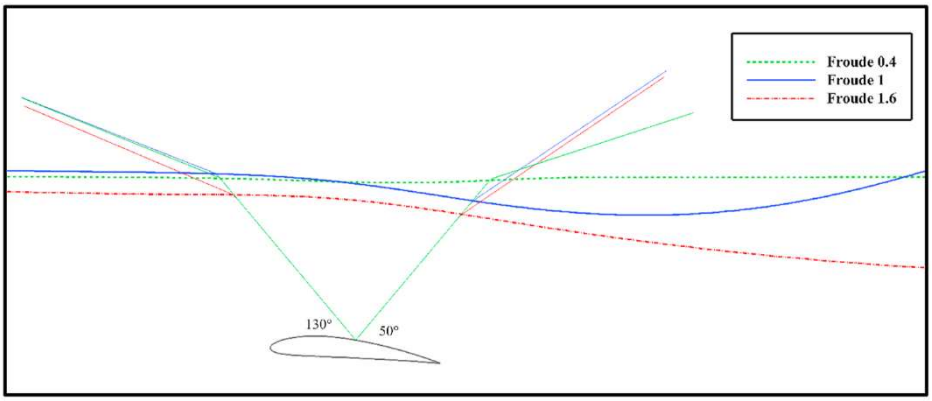

Fig. 37. Deflection patterns for NACA 4412 in AOA = 5, $h/c = 1$ in various Froude numbers and camera angles of 50° and 130° respectively.

Froude number decreases with sight decrease, and compared to the critical Froude number, velocity decreases with narrower sight, as Table 11 shows. Fig. 31, illustrates the different properties of the wave for Froude number transitions from 0.8 to 0.6 and finally 0.4 for the same case.

As the Froude number reduces, the wave appears flatter, as shown in Fig. 32. Moreover, a flatter wave gives less sight by changing the place and the angle of impact between the ray and the wave's surface. This will also affect the trend of deflection, as shown in Fig. 33.

According to Fig. 33, This alteration trend shows that as velocity increases and a wave is generated, the impact angle will change, and that phenomenon reduces the deflection amount, is not stable in the front area, and is mostly less at a lower speed.

4.4.2. *Super-critical froude number*

Similarly, when the Froude number increases in value by more than one, the flow is called a super-critical one in respect of the Froude number, and the previous steps will be followed again to observe the changing trends.

Based on Table 12, an increase of the Froude number firstly increases the sight in comparison with critical values by about 5%, but as the velocity grows in higher values, the sight slightly reduces but still delivers a bigger picture compared to the critical Froude number. This trend will also be investigated from the wave's shape and the deflection trend in Figs. 34 and 35, respectively.

According to Fig. 34, an increase in velocity will result in a wave with a higher length with an approximate identical amplitude. Obviously the wave's form is a dominance parameter on deflection and its trend is shown in Fig. 35.

According to Fig. 35, the window size decreases as the Froude number increases. Consequently, the greater the velocity results, the more significant the amount of deflection because of the various amplitude of waves.

Wave properties are determined by the distribution of dynamic pressure, as discussed previously. In addition to changing the wave's shape drastically, these changes in velocity also affect the wave's deflections. Moreover, according to Fig. 36, the amplitude of the wave and way of pressure distribution implies that changes in impact place between the ray and the wave's surface affect the amount of deflection and the size of the Snell's window, which is shown in Fig. 37.

Therefore, Fig. 37 can show the severity of deflection between 40° and 90° and the less significant one in front of the camera. The amount of deflection can be affected by the angle of impact between the ray and the water's surface, as well as by the length of the ray.

5. Conclusion

An incompressible two-dimensional simulation of a series of hydrofoils proceeding to the water's surface has been performed to extract the density field in the domain and capture the formed wave in several conditions. Obtaining resolved density-filed would compute fluctuating index-of-refraction filed through the Gladstone-Dale relation. The results include two main features affecting the amount of deflection: the formed wave due to variation of case studies and the ray length in the water zone. Unequivocally, the more hydrofoil is immersed in water, the more is the growth ray length and more minor alteration in the wave's shape. Consequently, the eyesight gains a vaguer vantage point as the window gets narrower, but the amount of deflection becomes lower as an advantage. On the other hand, one of the vital characteristics which are able to influence the wave's form is the angle of attack. Even though the window broadens by increasing the incidence angle on a larger scale, the deflection discrepancy contradicts one another in the front and beyond sight.

Furthermore, as the incidence angle increases, deflection decreases in the area behind but gets more in the other sight. Geometry is the last quality to be inspected, and it is proven that thicker hydrofoils are able to insignificantly expand the sight while the other geometrical parameter known as camber could have applied the same alterations but in a more notable way. The deflection trend in both cases is the same, where the deflections are more severe observing the front sight due to the ray impact angle to the wave's surface. As a result of increasing the flow's velocity, the sight will be enhanced for specific values, but more importantly, the deflections will be more significant with the increase. A reduced velocity, however, will lead to a flat wave, narrower sight, and more severe deflections.

CRediT authorship contribution statement

Shayan Rabizadeh: Conceptualization, Methodology, Software, Writing – original draft, Visualization, Investigation. **Ali Esmaeili:** Supervision, Data curation, Software, Writing – review & editing.

Declaration of competing interest

The authors declare that they have no known competing financial interests or personal relationships that could have appeared to influence the work reported in this paper.

Data availability

Data will be made available on request.

References

Ding, H., Yi, S., Zhu, Y., He, L., 2017. Experimental investigation on aero-optics of supersonic turbulent boundary layers. Appl. Opt. 56, 7604. https://doi.org/10.1364/ao.56.007604.

Djavareshkian, M.H., Esmaeili, A., 2014. Heuristic optimization of submerged hydrofoil using ANFIS-PSO. Ocean Eng. 92, 55–63. https://doi.org/10.1016/j.oceaneng.2014.09.033.

Djavareshkian, M.H., Esmaeili, A., 2013. Neuro-fuzzy based approach for estimation of Hydrofoil performance. Ocean Eng. 59, 1–8. https://doi.org/10.1016/j.oceaneng.2012.10.015.

Djavareshkian, M.H., Esmaeili, A., Parsania, A., 2013. Numerical simulation of smart hydrofoil in marine system. Ocean Eng. 73, 16–24. https://doi.org/10.1016/j.oceaneng.2013.07.015.

Earth, B., 2014. Bird vs fish | blue planet II [WWW Document]. URL. https://www.youtube.com/watch?v=h4pxLHG0Wzs.

Esmaeilifar, E., Hassan Djavareshkian, M., Forouzi Feshalami, B., Esmaeili, A., 2017. Hydrodynamic simulation of an oscillating hydrofoil near free surface in critical unsteady parameter. Ocean Eng. 141, 227–236. https://doi.org/10.1016/j.oceaneng.2017.06.037.

Field, M., 1994. Two-equation eddy-viscosity turbulence models for engineering applications. AIAA J. 32.

Garg, N., Pearce, B.W., Brandner, P.A., Phillips, A.W., Martins, J.R.R.A., Young, Y.L., 2019. Experimental investigation of a hydrofoil designed via hydrostructural optimization. J. Fluid Struct. 84, 243–262. https://doi.org/10.1016/j.jfluidstructs.2018.10.010.

Guo, G., Liu, H., Zhang, B., 2016. Aero-optical effects of an optical seeker with a supersonic jet for hypersonic vehicles in near space. Appl. Opt. 55, 4741. https://doi.org/10.1364/ao.55.004741.

Higton, D.K.L., S.Higton, S.A.D.K.L.. n.d. Encore - Snell's Window [WWW Document]. Oceanography. URL. https://epod.usra.edu/blog/2020/03/encore-snells-window.html. accessed 4.22.14.

Janssen, J., 1981. Searching for zooplankton just outside Snell's window. Limnol. Oceanogr. 26, 1168–1171. https://doi.org/10.4319/lo.1981.26.6.1168.

Kouh, J.S., Lin, T.J., Chau, S.W., n.d. Performance analysis of two-dimensional hydrofoil under free surface. J. Natl. Taiwan Univ. 86, 113–123.

Li, Z., Li, Y., Xing, B., Zhang, B., Tuo, H., Liu, H., 2019. OPD analysis and prediction in aero-optics based on dictionary learning. Aerosp. Syst. 2, 61–70. https://doi.org/10.1007/s42401-018-0020-1.

Shotorban, B., Zhang, M., Zhang, S., 2021. Aero Optical Effects over a Cylindrical Turret. https://doi.org/10.2514/6.2021-3125.

Sun, X.W., Liu, W., 2020. Validation case for supersonic boundary layer and turbulent aero-optical investigation in high-Reynolds-number freestream by WCNS-E-5. Proc. Inst. Mech. Eng. Part G J. Aerosp. Eng. 234, 2153–2166. https://doi.org/10.1177/0954410020932015.

Sun, X.W., Yang, X.L., Liu, W., 2021. Aero-optical and aero-heating effects of supersonic turbulent boundary layer with a tangential wall-injection film. Phys. Fluids 33. https://doi.org/10.1063/5.0044025.

Wang, M., Mani, A., Gordeyev, S., 2011. Physics and computation of aero-optics. Annu. Rev. Fluid Mech. 44, 299–321. https://doi.org/10.1146/annurev-fluid-120710-101152.

Xu, G.D., Xu, W.H., Duan, W.Y., Cai, H.P., Qi, J.T., 2020. The free surface effects on the hydrodynamics of two-dimensional hydrofoils in tandem. Eng. Anal. Bound. Elem. 115, 133–141. https://doi.org/10.1016/j.enganabound.2020.03.014.

Yang, B., Fan, Z., Yu, H., 2020. Aero-optical effects simulation technique for starlight transmission in boundary layer under high-speed conditions. Chin. J. Aeronaut. 33, 1929–1941. https://doi.org/10.1016/j.cja.2020.02.015.

Yang, B., Fan, Z., Yu, H., Hu, H., Yang, Z., 2021. A new method for analyzing aero-optical effects with transient simulation. Sensors 21, 1–28. https://doi.org/10.3390/s21062199.

Yu, J., Chen, S., Dang, F., Li, X., Shi, X., Wang, H., Fan, Z., 2021. The suppression of aero-optical aberration of conformal dome by wavefront coding. Opt Commun. 490 https://doi.org/10.1016/j.optcom.2021.126876.